

# The effect of local topography on the seismic response of a coupled train-bridge system

Hong Qiao<sup>1,2,3a</sup>, Xianting Du<sup>2b</sup>, He Xia<sup>\*2</sup>, Guido De Roeck<sup>3c</sup>, Geert Lombaert<sup>3d</sup> and Peiheng Long<sup>1e</sup>

<sup>1</sup>School of Civil and Transportation Engineering, Beijing University of Civil Engineering and Architecture, 15 Yongyuan Rd, Beijing 102616, China

<sup>2</sup>School of Civil Engineering, Beijing Jiaotong University, Shangyuancun No.3, Beijing 100044, China

<sup>3</sup>Department of Civil Engineering, KU Leuven, Kasteelpark Arenberg 40, Leuven B-3001, Belgium

(Received September 27, 2018, Revised November 22, 2018, Accepted December 19, 2018)

**Abstract.** The local topography has a significant effect on the characteristics of seismic ground motion. This paper investigates the influence of topographic effects on the seismic response of a train-bridge system. A 3-D finite element model with local absorbing boundary conditions is established for the local site. The time histories of seismic ground motion are converted into equivalent loads on the artificial boundary, to obtain the seismic input at the bridge supports. The analysis of the train-bridge system subjected to multi-support seismic excitations is performed, by applying the displacement time histories of the seismic ground motion to the bridge supports. In a case study considering a bridge with a span of 466 m crossing a valley, the seismic response of the train-bridge system is analyzed. The results show that the local topography and the incident angle of seismic waves have a significant effect on the seismic response of the train-bridge system. Leaving these effects out of consideration may lead to unsafe analysis results.

**Keywords:** train-bridge system; seismic analysis; topographic effect; viscous-spring artificial boundary; incident angle; azimuth

## 1. Introduction

In recent years, high-speed railway (HSR) networks are developing all over the world. These high speed lines contain a lot of multi-span elevated bridges. Since some of these bridges are located in seismic areas, the dynamic response of the train-bridge coupled system during earthquakes needs to be studied.

Since 1980s, many researchers have investigated this problem. Yang and Wu (2002) studied the dynamic stability of trains moving over bridges shaken by earthquakes with four typical earthquake records as excitations and found that the vertical component of ground motions could significantly influence the stability of the train-bridge coupled system. Zhang *et al.* (2010a) computed the non-stationary random responses of three-dimensional train-

bridge systems subjected to lateral horizontal earthquakes by combining the pseudo-excitation method and the precise integration method. Zeng and Dimitrakopoulos (2016) studied the seismic response of train vehicles crossing a horizontally curved railway bridge during frequent earthquakes and simulated the 3-D dynamics of a vehicle traveling on a curved path by using a moving trajectory system. In the aseismic design of long-span or long-extended bridges, it is important to take into account the variability of ground motion, which is due to wave traveling, incoherence and local site effects (Kiureghian and Neuenhofer 1992). In this regard, Xia *et al.* (2006) proposed an analysis model for train-bridge system subjected to seismic ground motion including the wave traveling effect. Yau and Frýba (2007) investigated the vibration of a suspension bridge due to moving loads and shaken by vertical support motions, in which the influence of seismic wave propagation effect was analyzed. Zhu *et al.* (2014) analyzed the dynamic behavior of a cable-stayed bridge simultaneously subjected to a moving train and seismic action, considering the influence of seismic wave propagation velocity. Du *et al.* (2012) proposed a framework for dynamic analysis of train-bridge system under non-uniform seismic ground motion, and studied the effect of wave traveling and spatial coherence on the dynamic responses of the train and the bridge. Although the local topography has an important effect on the features of seismic ground motion, its influence on the seismic response of train-bridge system has rarely been studied up to date.

In China, a lot of railway bridges are in operation or

---

\*Corresponding author, Professor

E-mail: [hxia88@163.com](mailto:hxia88@163.com)

<sup>a</sup>Lecturer

E-mail: [CarrieQh@163.com](mailto:CarrieQh@163.com)

<sup>b</sup>Associate professor

E-mail: [wadmdxt@163.com](mailto:wadmdxt@163.com)

<sup>c</sup>Professor

E-mail: [guido.deroeck@kuleuven.be](mailto:guido.deroeck@kuleuven.be)

<sup>d</sup>Professor

E-mail: [geert.lombaert@kuleuven.be](mailto:geert.lombaert@kuleuven.be)

<sup>e</sup>Professor

E-mail: [longpeiheng@bucea.edu.cn](mailto:longpeiheng@bucea.edu.cn)

under construction, and many of them are located in the southwestern region with mountainous site topographies and potential earthquakes. The most notorious one was the 2008 Wenchuan Earthquake with a magnitude 8, which caused damage to a large number of railway bridges (Wang 2008). Therefore, it is of great significance to study the seismic response of bridges located in these regions. In seismic analysis, it has long been recognized that the local topography has a non-negligible effect on the characteristics of seismic ground motion (Geli *et al.* 1988). Celebi (1987) found that in the Chile earthquake on 3 March 1985, structures located at ridges suffered more intensive damage than those at other places. Athanasopoulos *et al.* (1999) studied the non-uniform damage of the Greek town Egion during the 1995 Egion earthquake in terms of surface topography, and concluded that the surface topography influenced the intensity of base motion. Bi *et al.* (2010) studied the seismic response of a bridge frame located on a canyon site and found that local site conditions significantly affect spatial surface ground motions and hence the structural responses. Jia *et al.* (2015) investigated the characteristics and spatial distribution of structural damage based on the reconnaissance of buildings in Duijiangyan City during 2008 Wenchuan earthquake, and found that topography is one of the important factors leading to extraordinary spatial distribution of building damage. Since the local topography has a significant effect on the features of ground motion, seismic response of bridges located in such regions will be inevitably influenced. With regard to this aspect, there are also many studies (Rassem *et al.* 1996, Wang *et al.* 2008, Zhou *et al.* 2010, Jia *et al.* 2018). All these publications indicate the necessity of considering the topographic effect in seismic design, but few of them study this effect on the seismic response of train-bridge system. Since the characteristics of the train-bridge system differ from those of the empty bridge, findings from studies of bridges may not hold for the coupled system. This necessitates an extra study of the local topography on the seismic response of the train-bridge coupled system.

This paper presents a method for dynamic analysis of a train-bridge system subjected to earthquake action considering the local topography. The train-bridge system consists of the bridge submodel and the train submodel, established by the modal decomposition method and the rigid-body dynamics method, respectively, and linear wheel-track interaction (Zhang *et al.* 2010b) is adopted to connect the two submodels. The Newmark- $\beta$  method (Newmark 1959) is used to solve the motion equations. To take into account the topographic effect, a 3-D model is established for the local site represented by a viscous-spring artificial boundary and a finite element model. By transforming the seismic time histories into equivalent loads acting on the artificial boundary, the input at each support of the bridge considering topographic effect can be obtained after calculation. Then the dynamic analysis of a train-bridge system subjected to multi-point seismic excitation can be done, in which the displacement time histories of the seismic ground motion obtained by the above method are applied to the bridge supports. A train passing over a 466 m bridge located in a valley is taken as a case study, and the

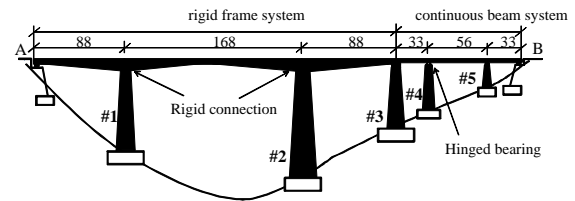


Fig. 1 Schematic view of the bridge (unit: m)

seismic response of the train-bridge system is analyzed considering local topography.

## 2. Description of the bridge

The southwestern region in China is a seismic zone susceptible to earthquakes. A railway bridge located in a V-shape valley in that region is considered, as shown in Fig. 1. The bridge with a total length of 466 m consists of a (88+168+88) m prestressed concrete (PC) continuous rigid frame system and a (33+56+33) m continuous PC box-girder.

The heights of the bridge piers from #1 to #5 are respectively 77 m, 103 m, 56 m, 46 m and 20 m, and the end abutments are marked as A and B, as shown in Fig. 1. The connections between the piers and the girder are sliding bearings except for the three marked in the figure.

In the following, the effect of the local topography on dynamic response of the train-bridge system during an earthquake is studied. The analysis procedure can be summarized as follows: first, the seismic excitation at each support of the bridge considering the topographic effects is obtained; then the analysis model of the train-bridge system subjected to seismic load is established, using the seismic excitation obtained in the previous step.

## 3. Ground motion considering local topography

### 3.1 FE modelling of local site

The finite element method has been used by many researchers to study seismic wave propagation and local site effects (Smith 1975, Assimaki and Gazetas 2004, Assimaki and Jeong 2013, Duzgun and Budak 2015, Zhao *et al.* 2017). However, it is necessary to extract a finite domain from the unbounded soil medium. In order to accurately model the originally continuous medium after extraction, the propagation characteristics of the soil should be kept unchanged, which necessitates an artificial boundary capable of absorbing the energy of the scattering waves. Both the viscous boundary (Lysmer and Kuhlemeyer 1969) and the viscous-spring artificial boundary (Du *et al.* 2006, Liu *et al.* 2006) are considered herein. Du and Zhao (2010) did analysis on the two-dimensional plane-strain Lamb problem to compare the two artificial boundaries and the results show that the viscous-spring artificial boundary has an acceptable accuracy while the viscous boundary leads to rigid-body displacement due to no stiffness constraint provided. Therefore, the modified viscous-spring artificial

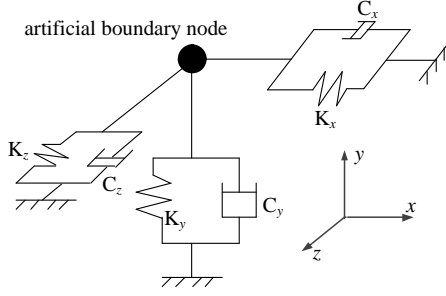


Fig. 2 Three-dimensional sketch of the adopted artificial boundary

boundary proposed by Du *et al.* (2006) is adopted here to establish the local site model. A three-dimensional sketch of the artificial boundary is shown in Fig. 2.

The parameters of the springs and dashpots constituting the artificial boundary can be obtained by the following equations (Du *et al.* 2006)

$$K_N = \frac{1}{1+\alpha} \cdot \frac{\lambda+2\mu}{r} \quad C_N = \beta\rho c_p \quad (1)$$

$$K_T = \frac{1}{1+\alpha} \cdot \frac{\mu}{r} \quad C_T = \beta\rho c_s \quad (2)$$

where the subscript N denotes the normal direction and T the tangential direction;  $\lambda$  and  $\mu$  are the Lamé constants;  $\rho$  is the mass density;  $r$  is the distance between the point load and the boundary, which takes the approximate value of the perpendicular distance from the center of the structure to the nodes of the boundary (Zhang *et al.* 2010c);  $c_p$  and  $c_s$  are the velocity of P-wave and S-wave, respectively, which are related to  $\mu$ ,  $\lambda$  and  $\rho$ ;  $\alpha$  and  $\beta$  are tuning coefficients, which can be obtained by numerical experiments. The recommended empirical values are  $\alpha=0.8$  and  $\beta=1.1$ .

The ANSYS software is used for establishing the model, in which the soil medium is modelled with Solid45 elements, and the springs and dampers of the artificial boundary are simulated by Combin14 elements with one end fixed.

### 3.2 Model of the incident seismic wave

The source of the incident wave lies outside the soil domain considered and far from the artificial boundary. According to Zhang *et al.* (2010c), the input motion can be converted into equivalent loads acting on the artificial boundary, to simulate the seismic wave input. Since the viscous-spring artificial boundary is responsible for absorbing the energy of scattering wave, the equivalent loads for simulating the free field consist of two components: one for balancing the force from springs and dashpots on the boundary, and another one for the stress field induced by free field wave motion. The equivalent loads in the normal and tangential directions can be expressed as

$$F_N = A \cdot [C_N \dot{u}_N(x, y, z, t) + K_N u_N(x, y, z, t) + \sigma_0(x, y, z, t)] \quad (3)$$

$$F_T = A \cdot [C_T \dot{u}_T(x, y, z, t) + K_T u_T(x, y, z, t) + \tau_0(x, y, z, t)] \quad (4)$$

where  $u_N(x, y, z, t)$  and  $u_T(x, y, z, t)$  are the normal and tangential displacements of the incident wave, respectively;  $\sigma_0(x, y, z, t)$  and  $\tau_0(x, y, z, t)$  are the normal and tangential stresses, respectively;  $x$ ,  $y$  and  $z$  are the node coordinates of the artificial boundary;  $A$  is the representative area of the node on the artificial boundary;  $K_N$ ,  $K_T$ ,  $C_N$  and  $C_T$  are the spring coefficients and damping coefficients in the normal and tangential directions, respectively. In a three-dimensional model, there are two tangential directions, which should be dealt with separately.

### 3.3 Calculation of equivalent loads

The propagating direction of incoming seismic waves can be described by the angle of incidence and the azimuth (which can be defined as the angle between the  $x$  axis and plane determined by incident wave and reflection wave) on the horizontal plane (Assimaki and Gazetas 2004). In existing studies, the angle of incidence has been studied more frequently because most of the local site models are two-dimensional (Wang *et al.* 2008, Zhou *et al.* 2010), in which the azimuth can only be zero. Assuming the P-wave propagates with incident angle  $\theta_1$  and azimuth  $\alpha$ , as shown in Fig. 3, the equivalent loads on the nodes of the artificial boundary can be obtained by Eqs. (3) and (4). The related items can be calculated by the following equations (Zhou 2009).

#### (1) Determination of the displacements

Taking the travel times of the waves into account, the displacement time histories at the left artificial boundary can be expressed as

$$u_L(t) = (u_0(t - \Delta t_1) \sin \theta_1 + \frac{A_2}{A_1} u_0(t - \Delta t_2) \sin \theta_1 \quad (5)$$

$$+ \frac{B_2 c_p}{A_1 c_s} u_0(t - \Delta t_3) \cos \theta_2) \cos \alpha$$

$$v_L(t) = u_0(t - \Delta t_1) \cos \theta_1 - \frac{A_2}{A_1} u_0(t - \Delta t_2) \cos \theta_1 \quad (6)$$

$$+ \frac{B_2 c_p}{A_1 c_s} u_0(t - \Delta t_3) \sin \theta_2$$

$$w_L(t) = (u_0(t - \Delta t_1) \sin \theta_1 + \frac{A_2}{A_1} u_0(t - \Delta t_2) \sin \theta_1 \quad (7)$$

$$+ \frac{B_2 c_p}{A_1 c_s} u_0(t - \Delta t_3) \cos \theta_2) \sin \alpha$$

those at the bottom artificial boundary expressed as

$$u_B(t) = u_0(t - \Delta t_7) \sin \theta_1 \cos \alpha \quad (8)$$

$$v_B(t) = u_0(t - \Delta t_7) \cos \theta_1 \quad (9)$$

$$w_B(t) = u_0(t - \Delta t_7) \sin \theta_1 \sin \alpha \quad (10)$$

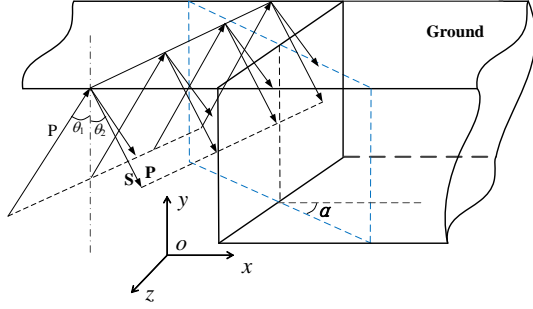


Fig. 3 Three-dimensional diagram of P-wave oblique incidence

and those at the rear artificial boundary expressed as

$$u_R(t) = (u_0(t - \Delta t_{10}) \sin \theta_1 + \frac{A_2}{A_1} u_0(t - \Delta t_{11}) \sin \theta_1 + \frac{B_2 c_p}{A_1 c_s} u_0(t - \Delta t_{12}) \cos \theta_2) \cos \alpha \quad (11)$$

$$v_R(t) = u_0(t - \Delta t_{10}) \cos \theta_1 - \frac{A_2}{A_1} u_0(t - \Delta t_{11}) \cos \theta_1 + \frac{B_2 c_p}{A_1 c_s} u_0(t - \Delta t_{12}) \sin \theta_2 \quad (12)$$

$$w_R(t) = (u_0(t - \Delta t_{10}) \sin \theta_1 + \frac{A_2}{A_1} u_0(t - \Delta t_{11}) \sin \theta_1 + \frac{B_2 c_p}{A_1 c_s} u_0(t - \Delta t_{12}) \cos \theta_2) \sin \alpha \quad (13)$$

where  $\theta_2$  represents the reflection angle of S-wave;  $A_2/A_1$  and  $B_2/A_1$  are the reflection coefficients of reflected P-wave and S-wave, respectively, expressed as

$$\frac{A_2}{B_1} = \frac{-2c_p^2 \sin 2\theta_1 \cos 2\theta_1}{c_s^2 \sin 2\theta_1 \sin 2\theta_2 + c_p^2 \cos^2 2\theta_1} \quad (14)$$

$$\frac{B_2}{B_1} = \frac{c_s^2 \sin 2\theta_2 \sin 2\theta_1 - c_p^2 \cos^2 2\theta_1}{c_s^2 \sin 2\theta_1 \sin 2\theta_2 + c_p^2 \cos^2 2\theta_1} \quad (15)$$

$\Delta t_1$  to  $\Delta t_3$  are the time lags of incident P-wave, reflected P-wave and reflected S-wave at the left boundary, respectively, expressed as

$$\Delta t_1 = \frac{y_L \cos \theta_1 + z_L \sin \theta_1 \sin \alpha}{c_p} \quad (16)$$

$$\Delta t_2 = \frac{y_L \cos \theta_1 + z_L \sin \theta_1 \sin \alpha}{c_p} + \frac{2(H - y_L) \cos \theta_1}{c_p} \quad (17)$$

$$\Delta t_3 = \frac{y_L \cos \theta_1 + z_L \sin \theta_1 \sin \alpha}{c_p} + \frac{H - y_L}{c_s \cos \theta_2} + \frac{(H - y_L) \cos(\theta_1 + \theta_2)}{c_p \cos \theta_2} \quad (18)$$

$\Delta t_7$  is the time lag of incident P-wave at the bottom boundary

$$\Delta t_7 = \frac{x_B \sin \theta_1 \cos \alpha + z_B \sin \theta_1 \sin \alpha}{c_p} \quad (19)$$

and  $\Delta t_{10}$  to  $\Delta t_{12}$  are the time lags of incident P-wave, reflected P-wave and reflected S-wave at the rear boundary, respectively, expressed as

$$\Delta t_{10} = \frac{x_R \sin \theta_1 \cos \alpha + y_R \cos \theta_1}{c_p} \quad (20)$$

$$\Delta t_{11} = \frac{x_R \sin \theta_1 \cos \alpha + y_R \cos \theta_1}{c_p} + \frac{2(H - y_R) \cos \theta_1}{c_p} \quad (21)$$

$$\Delta t_{12} = \frac{x_R \sin \theta_1 \cos \alpha + y_R \cos \theta_1}{c_p} + \frac{H - y_R}{c_s \cos \theta_2} + \frac{\cos(\theta_1 + \theta_2)(H - y_R)}{c_p \cos \theta_2} \quad (22)$$

where  $x$ ,  $y$ ,  $z$  are the coordinates of the nodes on each boundary;  $H$  represents the distance between the lower boundary and the ground surface.

When  $\alpha=0$ , the displacement time histories at the front artificial boundary are the same as those at the rear boundary.

## (2) Determination of the stresses

The stresses on the artificial boundaries are obtained from the governing elastodynamic equations (Timoshenko and Goodier 1970). For the left boundary,

$$\begin{aligned} \sigma_{Lx} = & \rho c_p \sin 2\theta_2 \cos^2 \alpha \frac{B_2}{A_1} \dot{u}_0(t - \Delta t_3) \\ & + \frac{\rho c_p [\nu + (1 - 2\nu) \sin^2 \theta_1 \cos^2 \alpha]}{1 - \nu} \dot{u}_0(t - \Delta t_1) \\ & + \frac{A_2 \rho c_p [\nu + (1 - 2\nu) \sin^2 \theta_1 \cos^2 \alpha]}{A_1 (1 - \nu)} \dot{u}_0(t - \Delta t_2) \end{aligned} \quad (23)$$

$$\begin{aligned} \tau_{Ly} = & \frac{G \sin 2\theta_1 \cos \alpha}{c_p} \dot{u}_0(t - \Delta t_1) \\ & - \frac{A_2}{A_1} \frac{G \sin 2\theta_1 \cos \alpha}{c_p} \dot{u}_0(t - \Delta t_2) \\ & - \rho c_p \cos 2\theta_2 \cos \alpha \frac{B_2}{A_1} \dot{u}_0(t - \Delta t_3) \end{aligned} \quad (24)$$

$$\begin{aligned} \tau_{Lz} = & \frac{G \sin^2 \theta_1 \sin 2\alpha}{c_p} \dot{u}_0(t - \Delta t_1) \\ & + \frac{A_2}{A_1} \frac{G \sin^2 \theta_1 \sin 2\alpha}{c_p} \dot{u}_0(t - \Delta t_2) \\ & - \rho c_p \sin 2\theta_2 \sin 2\alpha \frac{B_2}{2A_1} \dot{u}_0(t - \Delta t_3) \end{aligned} \quad (25)$$

for the bottom boundary,

$$\tau_{Bx} = \frac{G \sin 2\theta_1 \cos \alpha}{c_p} \dot{u}_0(t - \Delta t_7) \quad (26)$$

$$\sigma_{By} = \frac{\rho c_p [\nu + (1 - 2\nu) \cos^2 \theta_1]}{1 - \nu} \dot{u}_0(t - \Delta t_7) \quad (27)$$

$$\tau_{Bz} = \frac{G \sin 2\theta_1 \sin \alpha}{c_p} \dot{u}_0(t - \Delta t_7) \quad (28)$$

and for the rear boundary,

$$\begin{aligned} \tau_{Rx} &= \frac{G \sin^2 \theta_1 \sin 2\alpha}{c_p} \dot{u}_0(t - \Delta t_{10}) \\ &+ \frac{A_2}{A_1} \frac{G \sin^2 \theta_1 \sin 2\alpha}{c_p} \dot{u}_0(t - \Delta t_{11}) \\ &- \rho c_p \sin 2\theta_2 \sin 2\alpha \frac{B_2}{2A_1} \dot{u}_0(t - \Delta t_{12}) \end{aligned} \quad (29)$$

$$\begin{aligned} \tau_{Ry} &= \frac{G \sin 2\theta_1 \sin \alpha}{c_p} \dot{u}_0(t - \Delta t_{10}) \\ &- \frac{A_2}{A_1} \frac{G \sin 2\theta_1 \sin \alpha}{c_p} \dot{u}_0(t - \Delta t_{11}) \\ &- \rho c_p \cos 2\theta_2 \sin \alpha \frac{B_2}{A_1} \dot{u}_0(t - \Delta t_{12}) \end{aligned} \quad (30)$$

$$\begin{aligned} \sigma_{Rz} &= \frac{\rho c_p [\nu + (1 - 2\nu) \sin^2 \theta_1 \sin^2 \alpha]}{1 - \nu} \dot{u}_0(t - \Delta t_{10}) \\ &+ \frac{A_2}{A_1} \frac{\rho c_p [\nu + (1 - 2\nu) \sin^2 \theta_1 \sin^2 \alpha]}{1 - \nu} \dot{u}_0(t - \Delta t_{11}) \\ &+ \rho c_p \sin 2\theta_2 \sin^2 \alpha \frac{B_2}{A_1} \dot{u}_0(t - \Delta t_{12}) \end{aligned} \quad (31)$$

where the subscripts  $x, y, z$  denote the directions of stresses;  $\nu$  is the Poisson ratio of the soil; the meaning of other symbols is the same as previously mentioned. When  $\alpha=0$ , the stresses on the front artificial boundary have the same values but of opposite sign compared to those on the rear boundary.

By substituting Eqs. (5) to (31) into Eqs. (3) and (4), the equivalent loads acting on the artificial boundary can be obtained. Then the process of seismic wave propagating in the soil can be realized by applying these loads on the boundary.

#### 4. Verification of the input method

By a self-developed MATLAB program, the 3-D input procedure of P wave is implemented into the commercial software ANSYS. In this section, two numerical examples are presented to verify the input method.

##### 4.1 Numerical example 1

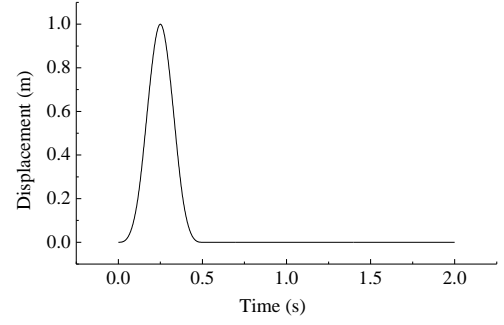


Fig. 4 Displacement time history of the incident P wave

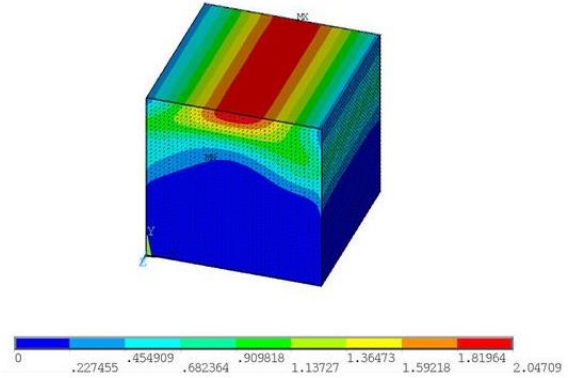


Fig. 5 Displacement contours of semi-infinite space under incident P wave at  $t=0.78$  s

Propagation process of P waves in a semi-infinite ground is first simulated using a truncated cube domain. The overall size of the region is  $2000 \text{ m} \times 2000 \text{ m} \times 2000 \text{ m}$  and the incident angle considered is  $30^\circ$ .

It is assumed that the medium has a mass density of  $2630 \text{ kg/m}^3$ , an elastic modulus of  $32.5 \text{ GPa}$  and a Poisson's ratio of  $0.22$ . The element size is set as  $50 \text{ m}$  (Lysmer and Kuhlemeyer 1969). An impulse (as plotted in Fig. 4) is adopted as the incident plane P wave and the time history of the impulse is defined as

$$\begin{aligned} u(t) &= 16u_0 \left[ G(t) - 4G\left(t - \frac{1}{8}\right) + 6G\left(t - \frac{1}{4}\right) \right. \\ &\quad \left. - 4G\left(t - \frac{3}{8}\right) + G\left(t - \frac{1}{2}\right) \right] \end{aligned} \quad (32)$$

$$G(t) = \left(\frac{t}{T_0}\right)^3 H\left(\frac{t}{T_0}\right) \quad (33)$$

where  $H(t)$  is the Heaviside function; the peak value of the impulse is  $1 \text{ m}$ ; and the acting time of the impulse  $T_0=0.5\text{s}$ .

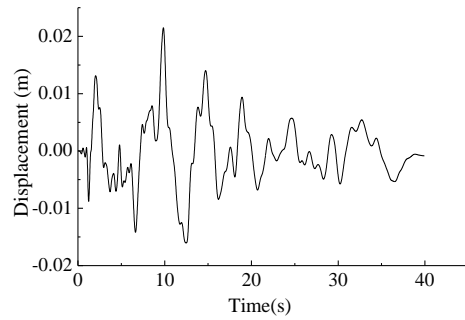
Fig. 5 shows the contours of displacement at time  $t=0.78$  s during the propagation process of the adopted P wave. It can be seen that the input method adopted in the paper can effectively simulate the propagation of P waves.

##### 4.2 Numerical example 2

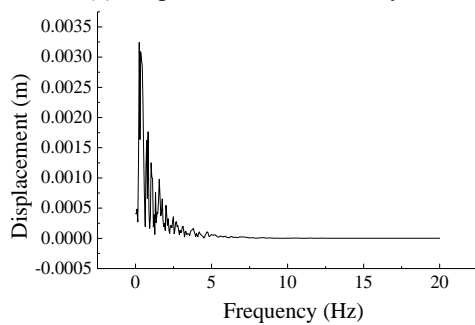
In this section, a simple cuboid model with an overall

Table 1 Parameters of the soil

Item	Parameters
Mass density	2610 kg/m <sup>3</sup>
Poisson's ratio	0.26
Elasticity modulus	5 GPa
Shear modulus	1.98 GPa
Velocity of P wave	1530 m/s
Velocity of S wave	871 m/s



(a) Displacement time history



(b) Displacement spectrum

Fig. 6 Characteristics of seismic ground motion

size of 624 m×160 m×120 m is taken as the second numerical example. The soil medium is assumed to be homogenous and isotropic, the parameters of which are shown in Table 1. Based on this model, a series of numerical tests are done to verify the application and accuracy of the input method.

First, a seismic wave, the characteristics of which are shown in Fig. 6, is assumed to be a plane P-wave traveling perpendicularly to the ground surface. It can be seen from Fig. 6(b) that the maximum frequency of the seismic wave is approximately 10 Hz, according to which the element size of the model is set as 4 m (Lysmer and Kuhlemeyer 1969). The calculated motions of the ground surface are compared with those obtained by EDT (Schevenels *et al.* 2009), a MATLAB toolbox for elastodynamic wave propagation in horizontally layered media based on the direct stiffness method and the thin layer method, as shown in Fig. 7. To reduce the calculation time, only part of the seismic wave is calculated.

It can be seen from Fig. 7 that when the wave travels perpendicularly to the ground surface, the results obtained by the input method agree well with those obtained by EDT. Even though there is some error which occurs probably due

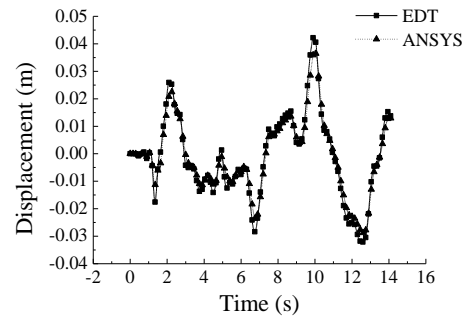


Fig. 7 Comparison between results obtained by ANSYS and EDT

Table 2 Amplification factors obtained by the method adopted and EDT

Incident angle	AF by the input method	AF by EDT	Relative error
0°	2.008	2	0.4%
30°	1.702	1.697	0.3%
45°	1.378	1.374	0.3%
60°	1.019	1.017	0.2%

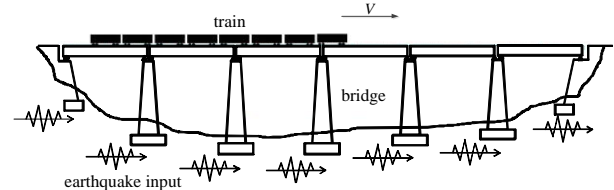


Fig. 8 Train-bridge system subjected to earthquake action

to the relatively large element size, considering the huge computation cost, the results are sufficiently accurate for seismic analysis of bridge structures.

Then a sinusoidal wave with its frequency equal to 2 Hz is assumed to travel with different incident angles to the ground surface. Table 2 shows the amplification factors (AF) defined as the ratio of the vertical motion at the surface to the amplitude of the incident sinusoidal wave, which are obtained by the input method and EDT respectively.

It can be seen that when different incident angles are considered, accurate results can still be obtained by the input method.

Finally, through the above two numerical examples, the application and accuracy of the input method adopted in the paper have been verified.

## 5. Analysis model of train-bridge system during earthquakes

The train-bridge system subjected to earthquake excitation is shown in Fig. 8, which is composed of the train submodel, the bridge submodel, and the earthquake input.

The seismic load only acts on the bridge submodel, whose influence on the train submodel is realized by the wheel-track interacting forces. In establishing the motion

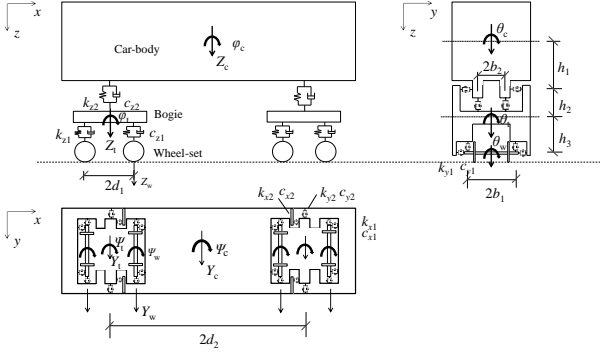


Fig. 9 The vehicle element model

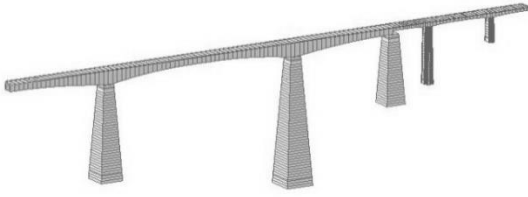


Fig. 10 Finite element model of the bridge

equations of these two submodels considering non-uniform seismic input, several assumptions are made:

(1) The train submodel consists of several independent vehicles;

(2) Each vehicle element consists of a car-body, two bogies and four wheel-sets, which are connected by spring-and-dashpot suspension systems (Xia 2011), as shown in Fig. 9 A multiple-degree-of-freedom system is employed to represent each vehicle (Du *et al.* 2012);

(3) The train passes through the bridge with a constant speed.

In absolute coordinates, the dynamic motion equations of the train and bridge submodels can be expressed by Eqs. (34) and (35), respectively.

$$\mathbf{M}_V \ddot{\mathbf{u}}_V + \mathbf{C}_V \dot{\mathbf{u}}_V + \mathbf{K}_V \mathbf{u}_V = \mathbf{F}_{V,B} \quad (34)$$

$$\begin{bmatrix} \mathbf{M}_{ss} & \mathbf{M}_{sb} \\ \mathbf{M}_{bs} & \mathbf{M}_{bb} \end{bmatrix} \begin{Bmatrix} \ddot{\mathbf{u}}_s \\ \ddot{\mathbf{u}}_b \end{Bmatrix} + \begin{bmatrix} \mathbf{C}_{ss} & \mathbf{C}_{sb} \\ \mathbf{C}_{bs} & \mathbf{C}_{bb} \end{bmatrix} \begin{Bmatrix} \dot{\mathbf{u}}_s \\ \dot{\mathbf{u}}_b \end{Bmatrix} + \begin{bmatrix} \mathbf{K}_{ss} & \mathbf{K}_{sb} \\ \mathbf{K}_{bs} & \mathbf{K}_{bb} \end{bmatrix} \begin{Bmatrix} \mathbf{u}_s \\ \mathbf{u}_b \end{Bmatrix} = \begin{Bmatrix} \mathbf{F}_{B,V} \\ \mathbf{0} \end{Bmatrix} \quad (35)$$

where  $\mathbf{M}$ ,  $\mathbf{C}$ ,  $\mathbf{K}$  are the mass, damping and stiffness matrices, respectively; the subscripts B and V denote the bridge submodel and the train submodel;  $\mathbf{u}$ ,  $\dot{\mathbf{u}}$  and  $\ddot{\mathbf{u}}$  represent the displacement, velocity and acceleration vectors, respectively; the displacement vector of the bridge  $\mathbf{u}_B$  is decomposed into  $\mathbf{u}_s$  and  $\mathbf{u}_b$ , which denote the displacements of the superstructure and base of the bridge, respectively.  $\mathbf{F}_{V,B}$  and  $\mathbf{F}_{B,V}$  are the interaction forces between the bridge submodel and the train submodel, which are determined by the analysis model of wheel-rail contact relationship.

When combining the train submodel and the bridge

submodel based on certain wheel-rail contact relationship, the rail irregularity is an important factor. It reflects the relative displacement between the wheel and rail and can cause additional velocity and acceleration, which can be expressed in a differential form (Zhang *et al.* 2010b)

$$\dot{E} = \lim_{\Delta t \rightarrow 0} \frac{\Delta E}{\Delta t} = \lim_{\Delta t \rightarrow 0} \frac{\Delta E}{\Delta X / V} = V \cdot \lim_{\Delta t \rightarrow 0} \frac{\Delta E}{\Delta X} = V \cdot \frac{\partial E}{\partial X} \quad (36)$$

$$\ddot{E} = \lim_{\Delta t \rightarrow 0} \frac{\Delta \dot{E}}{\Delta t} = \lim_{\Delta t \rightarrow 0} \frac{\Delta \dot{E}}{\Delta X / V} = V \cdot \lim_{\Delta t \rightarrow 0} \frac{\Delta \dot{E}}{\Delta X} = V^2 \cdot \frac{\partial^2 E}{\partial X^2} \quad (37)$$

where  $E$  is the relative displacement between the wheel and rail and  $V$  is the train speed.

In this paper, to determine  $\mathbf{F}_{V,B}$  and  $\mathbf{F}_{B,V}$ , the wheel-rail ‘‘corresponding assumption’’ and the simplified Kalker creep theory (Zhang *et al.* 2010b) are chosen to define the vertical and lateral interactions respectively, which mean:

(1) For the vertical interaction between the wheel and rail, the wheel-set motion is the sum of the bridge deck motion and additional motion caused by irregularity;

(2) In the lateral direction, the wheel-rail interacted forces are defined by the Kalker creep theory, but to maintain the linear relationship between the relative motion and interacting force, the following assumptions are adopted:

(a) The wheel is a cone surface at the contact point.

(b) The rail is a cylindrical surface with 300 mm radius.

(c) The wheel-rail normal interacting force is regarded as the static wheel weight.

(d) The coupling of  $Y$  and  $R_Z$  motion of the wheel-set is neglected, as shown in Fig. 9.

Comprehensive derivation procedure and specific expressions of  $\mathbf{F}_{V,B}$  and  $\mathbf{F}_{B,V}$  can be found in Zhang *et al.* (2010b), which are not given here for lack of space.

On the other hand, the first equation in Eq. (35) is for the bridge superstructure, which can be written with respect to the absolute displacement at the base as

$$\mathbf{M}_{ss} \ddot{\mathbf{u}}_s + \mathbf{C}_{ss} \dot{\mathbf{u}}_s + \mathbf{K}_{ss} \mathbf{u}_s = -\mathbf{K}_{sb} \mathbf{u}_b - \mathbf{C}_{sb} \dot{\mathbf{u}}_b - \mathbf{M}_{sb} \ddot{\mathbf{u}}_b + \mathbf{F}_{B,V} \quad (38)$$

The third item on the right side of Eq. (38) becomes zero if a lumped mass matrix is used for the bridge, so Eq. (38) can be rewritten as

$$\mathbf{M}_{ss} \ddot{\mathbf{u}}_s + \mathbf{C}_{ss} \dot{\mathbf{u}}_s + \mathbf{K}_{ss} \mathbf{u}_s = -\mathbf{K}_{sb} \mathbf{u}_b - \mathbf{C}_{sb} \dot{\mathbf{u}}_b + \mathbf{F}_{B,V} \quad (39)$$

The second item on the right side of the equation stands for the damping loading due to ground motion, which can be neglected (Wilson 2002). Then by applying the modal decomposition method, Eq. (39) is converted in a set of independent modal equations (Tsai 1998), namely,

$$\ddot{q}_i + 2\xi_i \omega_i \dot{q}_i + \omega_i^2 q_i = \boldsymbol{\phi}_i^T \mathbf{M}_{ss} \mathbf{R}(\omega_i^2 \mathbf{u}_b) + \boldsymbol{\phi}_i^T \mathbf{F}_{B,V} \quad (i = 1, 2, \dots, n) \quad (40)$$

where  $\boldsymbol{\phi}_i$  and  $q_i$  are the  $i$ th normalized mode shape and generalized coordinate,  $\omega_i$  is the  $i$ th circular frequency;  $n$  is the number of the modes concerned;  $\mathbf{R}$  is the so-called displacement influence matrix, expressed as

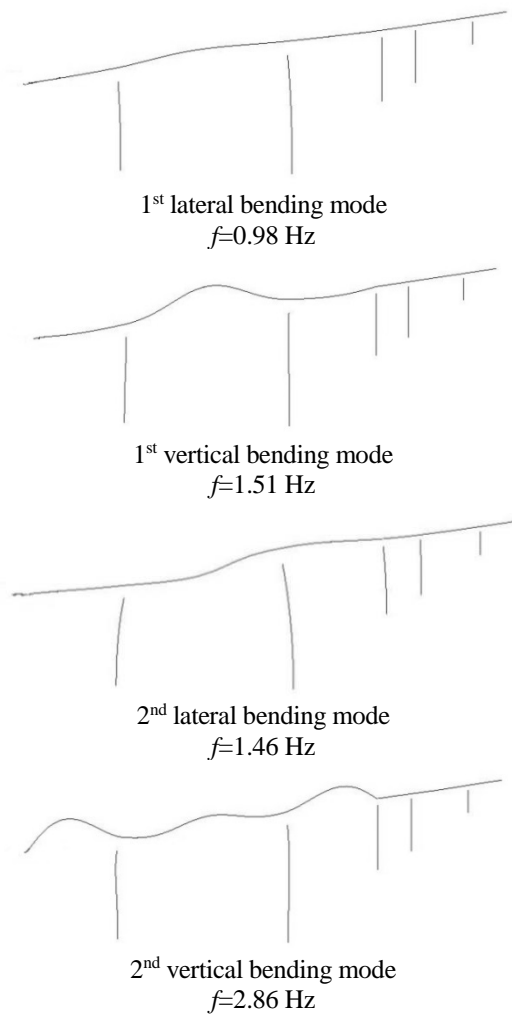


Fig. 11 Natural frequencies and mode shapes of the bridge

$$\mathbf{R} = -\mathbf{K}_{ss}^{-1}\mathbf{K}_{sb} \quad (41)$$

Eqs. (34) and (40) are the basic motion equations for the train-bridge system subjected to seismic ground motion, which are connected by a wheel-track interaction relationship. The motion equations are solved by the time integration method.

## 6. Case study

### 6.1 Bridge and train

The railway bridge mentioned in Section 2 is taken as the case study. A 3-D FE model of the bridge is established, using beam elements to model the frame, the girder and the piers, as shown in Fig. 10. Four dominant natural frequencies and the corresponding mode shapes are shown in Fig. 11. The concrete parameters of the beam are as follows: the elastic modulus is 36 GPa and the density is 2650 kg/m<sup>3</sup>.

The first 80 modes covering the frequency interval 0.8 Hz to 23 Hz are used for analysis of the bridge, and the adopted damping ratio is 0.025 according to previous measurement

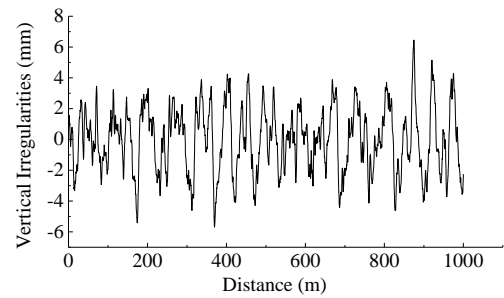


Fig. 12 The vertical irregularity curve

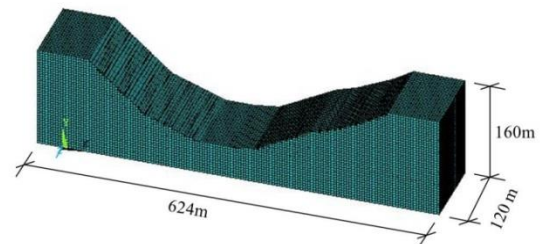


Fig. 13 Finite element model of the local topography

results (Xia *et al.* 2005).

A high-speed train with 8 cars (the fourth and the eighth are trailers and the others are motors) is taken as the train model and its major parameters are shown in Table 3. The motion equation of the train model is assembled according to Xia *et al.* (2011).

The track irregularities are taken into account by using measured data, of which the vertical component is shown in Fig. 12.

### 6.2 The local topography and seismic input

The bridge is located in a V-shaped valley, which finite element model is established in ANSYS, as shown in Fig. 13.

The soil medium is assumed to be homogenous and isotropic, the parameters of which are shown in Table 1. The overall size of the model is 624 m×160 m×120 m and the element size is 4 m, as illustrated in the numerical example 2 in Section 4. The Solid 45 element (a 3-D structural solid element with 8 nodes) is used to model the soil medium, and the Combin 14 element (a spring-damper element) for the viscous-spring artificial boundary.

In the analysis, the seismic ground motion record shown in Fig. 6 is used as the seismic excitation. With the assumption that the incident seismic wave is a plane P-wave, the corresponding equivalent loads acting on the artificial boundary can be obtained by Eqs. (3) to (31). By applying the equivalent loads on the artificial boundary, the propagating seismic waves are simulated, resulting in the non-uniform seismic excitations at all supports for the seismic analysis of the train-bridge system.

### 6.3 Simulation results

The dynamic response of the train-bridge system is studied for different cases, without/with seismic excitation and considering/neglecting the topographic effects,

Table 3 Main parameters of the train submodel

Item	Unit	Motor car	Trailer car
Mass of car-body	kg	$4.8 \times 10^4$	$4.4 \times 10^4$
Mass of bogie	kg	$3.2 \times 10^3$	$2.4 \times 10^3$
Mass of wheel set	kg	$2.4 \times 10^3$	$2.4 \times 10^3$
Rolling inertia moment of car-body	$\text{kg} \cdot \text{m}^2$	$1.15 \times 10^5$	$1.0 \times 10^5$
Pitching inertia moment of car-body	$\text{kg} \cdot \text{m}^2$	$2.7 \times 10^6$	$2.7 \times 10^6$
Yawing inertia moment of car-body	$\text{kg} \cdot \text{m}^2$	$2.7 \times 10^6$	$2.7 \times 10^6$
Rolling inertia moment of bogie	$\text{kg} \cdot \text{m}^2$	$3.2 \times 10^3$	$1.8 \times 10^3$
Pitching inertia moment of bogie	$\text{kg} \cdot \text{m}^2$	$7.2 \times 10^3$	$2.2 \times 10^3$
Yawing inertia moment of bogie	$\text{kg} \cdot \text{m}^2$	$6.8 \times 10^3$	$2.2 \times 10^3$
Rolling inertia moment of wheel-set	$\text{kg} \cdot \text{m}^2$	$1.2 \times 10^3$	$1.1 \times 10^3$
Yawing inertia moment of wheel-set	$\text{kg} \cdot \text{m}^2$	$1.2 \times 10^3$	$1.1 \times 10^3$
Vertical stiffness of primary suspension	N/m	$1.04 \times 10^6$	$0.7 \times 10^6$
Vertical damping of primary suspension	N·s/m	$4 \times 10^4$	$4 \times 10^4$
Lateral stiffness of primary suspension	N/m	$3 \times 10^6$	$5 \times 10^6$
Lateral damping of primary suspension	N·s/m	0	0
Vertical stiffness of secondary suspension	N/m	$4 \times 10^5$	$3 \times 10^5$
Vertical damping of secondary suspension	N·s/m	$5 \times 10^4$	$5 \times 10^4$
Lateral stiffness of secondary suspension	N/m	$2.4 \times 10^5$	$2.8 \times 10^5$
Lateral damping of secondary suspension	N·s/m	$3 \times 10^4$	$2.5 \times 10^4$
Full length of vehicle	m	24.775	24.775
Distance between two bogies in a vehicle	m	17.375	17.375
Distance between axles on a bogie	m	2.5	2.5

respectively, to analyze the influence of the local topography on the seismic response of train-bridge system. In the case where the local topography is not considered, the free horizontal surface is taken as the upper surface of the model (Wang 2008).

The influence of the incident angle and the azimuth on the dynamic response of the bridge and the running safety of the train is studied, considering values of  $0^\circ$ ,  $30^\circ$ ,  $45^\circ$ ,  $60^\circ$  and  $0^\circ$ ,  $30^\circ$ ,  $45^\circ$ ,  $90^\circ$  for the incident angle and the azimuth, respectively.

Since only an incident P-wave is considered in the following, the vertical response components will generally be larger than the horizontal ones.

### 6.3.1 Comparison between considering and neglecting topographic effects

Firstly, a finite element model of the local topography without the bridge has been established and the incident P wave is assumed to travel perpendicularly to the ground surface. Table 4 shows the peak values of vertical ground motion where the bridge supports are located. Corresponding peak values without the local topography being considered are also given for comparison. It can be seen that the amplitudes increase up to 22% when the local topography is taken into account.

With the assumption that the earthquake occurs when the train enters the bridge, displayed in Fig. 14 are the displacement time histories at the mid of the second span (the longest span) of the bridge with and without earthquake

Table 4 Peak values of vertical ground motion where the bridge supports are located (Unit: m)

	Topography considered	Topography neglected	Increment
A	0.040	0.036	+11%
#1	0.034	0.036	-6%
#2	0.044	0.036	+22%
#3	0.039	0.036	+8%
#4	0.038	0.036	+6%
#5	0.040	0.036	+11%
B	0.041	0.036	+14%

action, and with and without consideration of the local topography. The incident seismic wave is assumed to be the plane P-wave travelling perpendicularly to the ground surface, and the train speed is 250 km/h.

It can be seen from the figure that under the earthquake excitation the dynamic response of the bridge highly increases. In addition, it is observed that the topography has an important effect on the seismic response of the train-bridge system. Accounting for the topographic effects leads to a larger vertical displacement of the bridge which is 3.16 times larger than in case these effects are disregarded. The topography also affects the time at which the peak value of the displacement is obtained, as the local topography changes the arrival time of the seismic wave to the ground surface. The topography has an even more pronounced

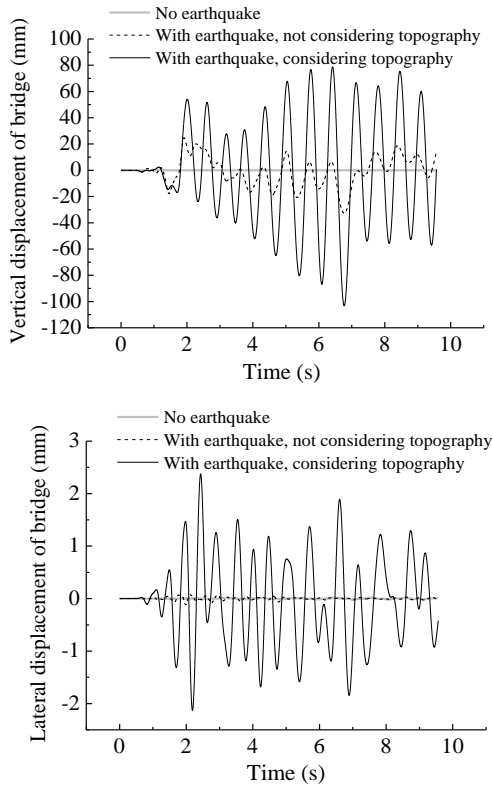


Fig. 14 Displacement time histories of the bridge under various conditions

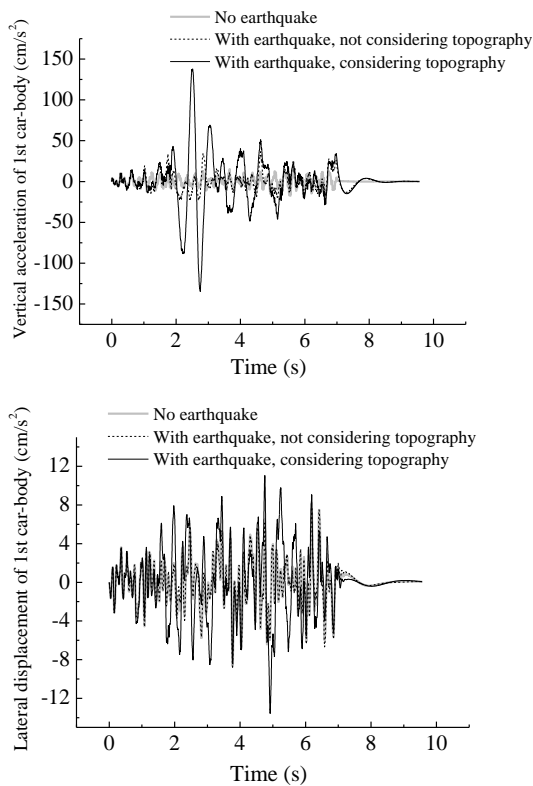


Fig. 15 Acceleration time histories of 1st car-body under various conditions

effect on the lateral displacement which is considerably

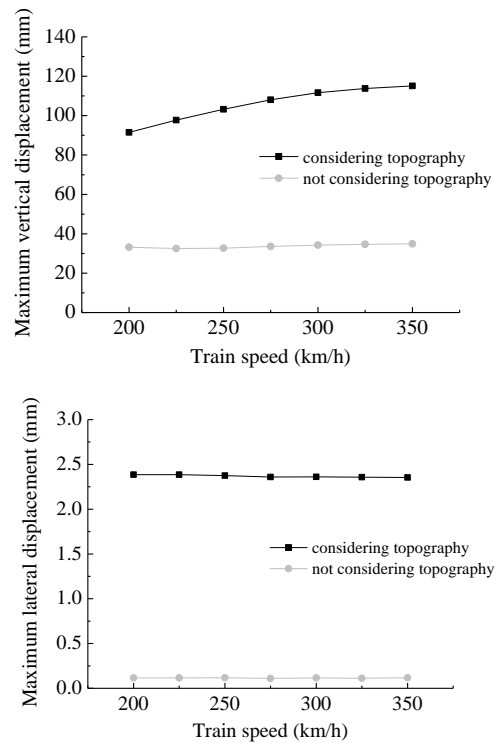


Fig. 16 Comparison of maximum bridge displacements with/without considering topography

larger than in the case where it is not considered.

Fig. 15 shows the vertical and lateral acceleration time histories of the 1<sup>st</sup> car-body under the same conditions. It can be seen from the figure that when the topographic effect is considered, the maximum vertical and lateral car-body accelerations are 1.38 m/s<sup>2</sup> and 0.14 m/s<sup>2</sup>. So, they respectively increased by 3.77 and 1.54 times.

Figs. 16 and 17 show how the maximum value of the displacement of the second mid-span and the acceleration of the 1<sup>st</sup> car-body, respectively, change with the train speed. It can be seen from these figures that when the local topography is considered, the maximum responses of all the items increased.

### 6.3.2 Influence of time of occurrence of earthquake

An earthquake may happen at any time when a train crosses a long-span bridge, and the time of occurrence may significantly affect the seismic response of train-bridge system. In order to study this influence, four typical cases are selected for comparison, as illustrated in Fig. 18.

In Case 1, the earthquake occurs when the train enters onto the bridge. In Case 2, the earthquake occurs when the train arrives at the mid-span of the first span of the bridge. In Case 3, the earthquake occurs when the first vehicle enters the longest span. In Case 4, the earthquake occurs when the whole train is just on the bridge.

With the assumption that the train speed is 250 km/h, the results for all the above four cases are shown in Table 5. The running safety is determined by the offload factor and the derailment factor. The offload factor  $f_{off}$  and the derailment factor  $f_{der}$  are defined following Xia *et al.* (2011) as

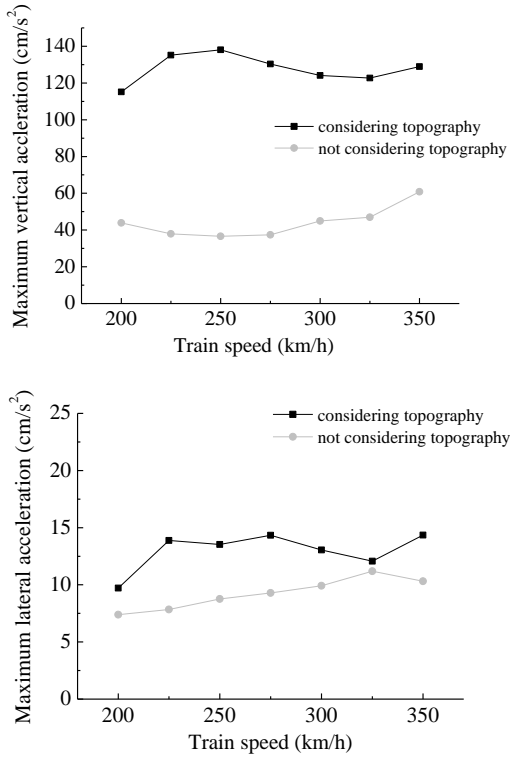


Fig. 17 Comparison of maximum car-body accelerations with/without considering topography

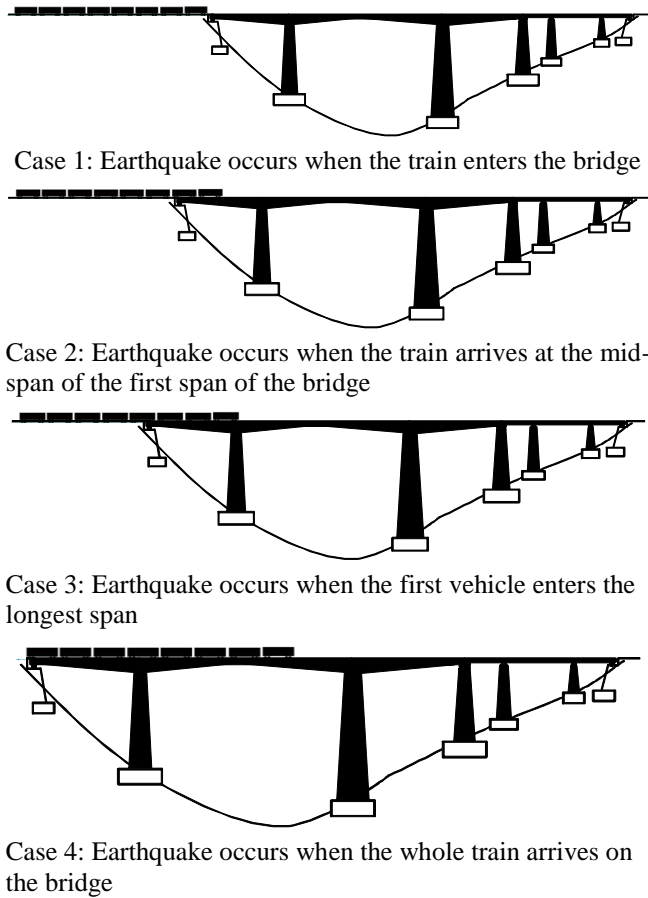


Fig. 18 Cases of different occurrence time of earthquake

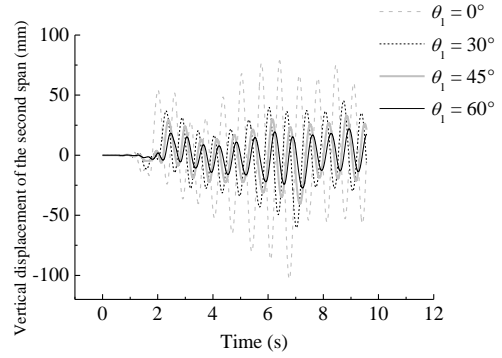


Fig. 19 Vertical displacement time histories of the bridge under different incident angles

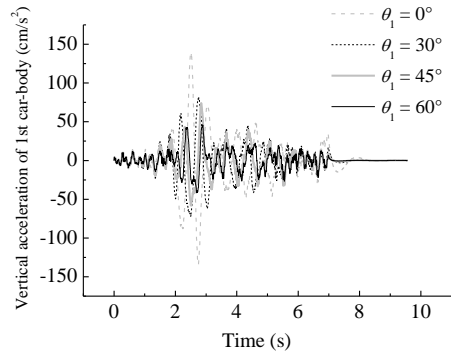


Fig. 20 Vertical acceleration time histories of 1st car-body under different incident angles

$$f_{\text{off}} = \Delta P / P_{\text{static}} \quad (42)$$

$$f_{\text{der}} = Q / P \quad (43)$$

where  $P_{\text{static}}$  is the average static wheel load;  $P$  is the dynamic wheel load;  $\Delta P$  is the offloaded wheel load, which can be defined as the difference between  $P_{\text{static}}$  and  $P$ ;  $Q$  is the lateral force acting on the wheel.

It can be seen that for the four cases, the dynamic response of the train-bridge system during earthquakes is different, which demonstrates that the occurrence time of earthquake has an influence on the seismic response of train-bridge system. However, the results in Table 5 also indicate that there are no obvious patterns among these responses. Since the running safety is the most significant concern in train-bridge dynamic analysis, the situation in Case 1 with the largest offload and derailment factor among the four cases, is adopted for the following analysis.

### 6.3.3 Influence of incident angle and azimuth

#### (1) Influence of incident angle

Shown in Figs. 19 and 20 are the vertical displacement time histories of the second span of the bridge and the vertical acceleration time histories of the 1<sup>st</sup> car-body, which are calculated at the train speed of 250 km/h, under the conditions of zero azimuth but different incident angles for the earthquake excitation. It can be seen that with the increase of incident angle, both the bridge displacement and the car-body acceleration are decreasing. This is because at

Table 5 Maximum dynamic response of train-bridge system for the 4 cases with different time of occurrence of earthquake

Occurrence time	Displacement of the second mid-span of the bridge (mm)		Acceleration of the 1 <sup>st</sup> car-body (cm/s <sup>2</sup> )		Offload factors of all vehicles	Derailment factors of all vehicles
	Vertical	Lateral	Vertical	Lateral		
Case 1	103.25	2.37	138.03	13.54	0.78	0.60
Case 2	109.78	2.36	123.98	12.85	0.65	0.36
Case 3	114.18	2.35	124.17	13.44	0.65	0.38
Case 4	99.70	2.36	144.20	12.07	0.68	0.50

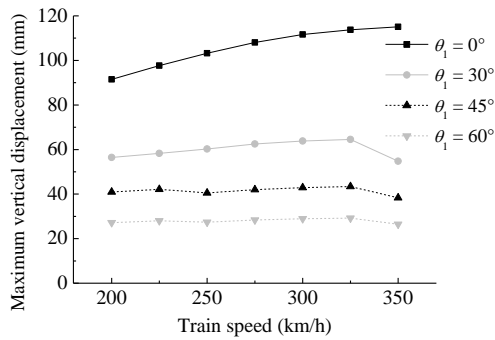


Fig. 21 Maximum vertical bridge displacement as a function of the train speed for different incident angles

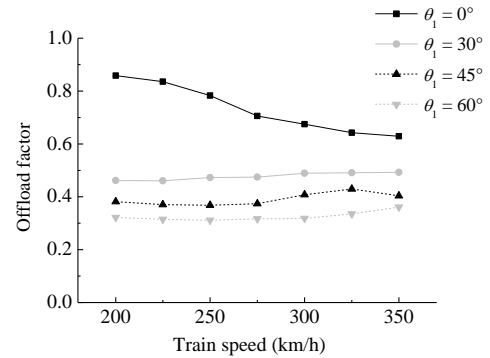


Fig. 23 Maximum offload factors of train as a function of the train speed for different incident angles

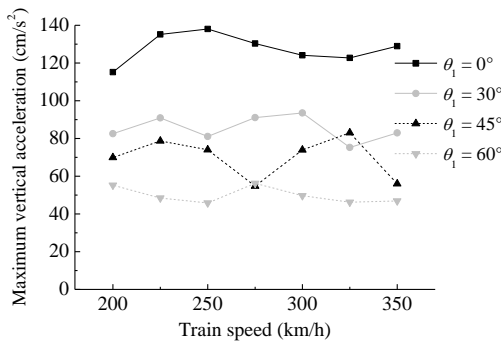


Fig. 22 Maximum vertical car-body acceleration as a function of the train speed for different incident angles

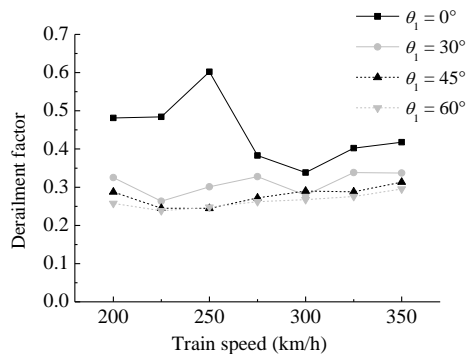


Fig. 24 Maximum derailment factors of train as a function of the train speed for different incident angles

a given azimuth, the vertical component of ground motion becomes smaller for the larger incident angle. It can also be found from the figures that the variation of incident angle also leads to the time delay of the dynamic responses, due to the change of arrival time of seismic wave at the ground surface.

Shown in Figs. 21 and 22 are the distributions of maximum vertical displacements of the second mid-span of the bridge and the vertical accelerations of the 1<sup>st</sup> car-body under several incident angles, as a function of train speed, and in Figs. 23 and 24 are the distributions of maximum offload factors and derailment factors taken from all the wheel/rail forces of the train vehicles, all under zero azimuth condition.

It can be seen that the four quantities show a different dependence on the train speed and generally decrease with an increasing angle of incidence.

(2) Influence of azimuth

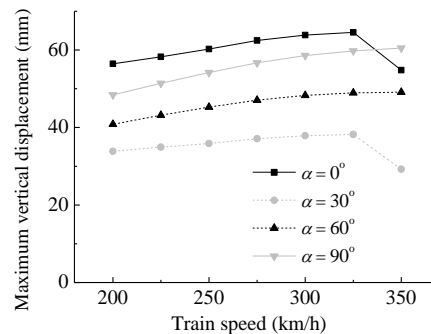


Fig. 25 Maximum vertical bridge displacement as a function of the train speed for different azimuths

The influence of the azimuth is studied, considering values of 0°, 30°, 45° and 90° while keeping the angle of

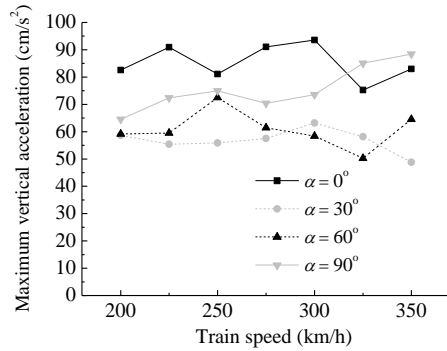


Fig. 26 Maximum vertical car-body acceleration as a function of the train speed for different azimuths

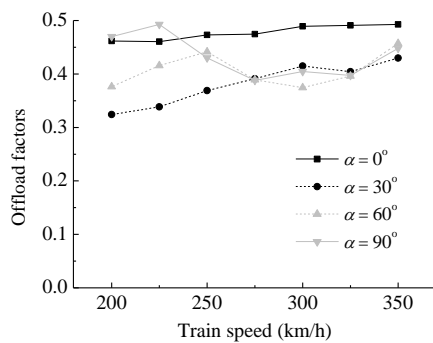


Fig. 27 Maximum offload factors of train as a function of the train speed for different azimuths

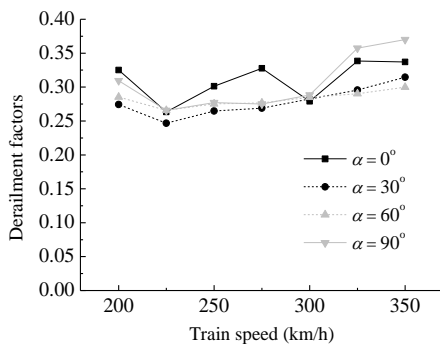


Fig. 28 Maximum derailment factors of train as a function of the train speed for different azimuths

incidence equal to 30°. Shown in Figs. 25 and 26 are the maximum vertical bridge displacement and the vertical car-body acceleration, as a function of train speed, and in Figs. 27 and 28 are the maximum offload factors and the derailment factors of the train under different train speeds.

It can be seen that compared to the incident angle, the influence of the azimuth is more complex. In general, for an incident angle=30°, the azimuths equal to 0 and 90° lead to larger seismic responses of the train-bridge system. Since a 2D model, often considered in practice, is only able to consider the condition with zero azimuth, such a model may yield unsafe results.

(3) Combined influence of incident angle and azimuth

Shown in Table 6 are the maximum dynamic responses of train-bridge system with respect to different incident angles and azimuths, when the train speed is 200 km/h, 250 km/h, 300 km/h, respectively.

From Table 6(a), it can be seen that, for all azimuth angles, the maximum vertical bridge displacement and 1<sup>st</sup> car body acceleration decreases with an increasing incident angle, and so do most of the maximum offload factors in Table 6(b). This is because the vertical component of ground motion becomes smaller for larger incident angles and the offload factor is mainly determined by the vertical wheel-rail force according to Eq. (42).

By contrast, however, there is no clear trend showing how the dynamic responses of a train-bridge system change with the azimuth for a given incident angle. The values in bold are the maxima under certain incident angle and train speed. It can be seen that dynamic responses of the train-bridge system obtained under other azimuths can be larger than those with zero azimuth in most cases, thus a 3-D model is required to analyze the effects of local topography on the seismic response of train-bridge system.

7. Conclusions

In this paper, the influence of local topography is studied for the response of a train-bridge system subjected to an incident P-wave. The results of a case study considering different values of the incident angles and azimuths of seismic P-waves allow drawing the following conclusions:

- Seismic excitation can considerably increase the dynamic response of train-bridge system, thus it is important to study its dynamic behavior during earthquakes.
- Local topography has a non-negligible effect on the seismic response of train-bridge system, and when disregarded, this may lead to underestimation of the dynamic response of the system during earthquakes.
- Both the incident angle and the azimuth affect the seismic response of the train-bridge system and for this reason, the case study demonstrates that a 3-D model is required to analyze the effects of local topography on the seismic response of the coupled system.

It should be pointed that in this analysis, for lack of space, only the influence of the incident P wave is analyzed, while the input method used in the paper is also suitable for the S wave, and related studies will be given in the future. Moreover, the soil in the case study is assumed to be homogenous and isotropic. It is hoped that in the future further research on heterogeneous soil can be performed.

In the next stage of study, the authors will also try to find a more representative rule to determine the critical incident angle and azimuth, which is important for considering the influence of local topography on the seismic response of the train-bridge system.

Acknowledgments

This research was carried out when the first author worked as a visiting scholar at KU Leuven sponsored by

Table 6 Maximum dynamic responses of train-bridge system under different incident angles and azimuths

(a) Vertical displacements of the second mid-span of the bridge and accelerations of the 1st car-body								
V=200 km/h								
	Vertical displacement of the second mid-span of the bridge (mm)				Vertical acceleration of the 1 <sup>st</sup> car-body (cm/s <sup>2</sup> )			
	$\alpha=0$	$\alpha=30^\circ$	$\alpha=60^\circ$	$\alpha=90^\circ$	$\alpha=0$	$\alpha=30^\circ$	$\alpha=60^\circ$	$\alpha=90^\circ$
$\theta_1=30^\circ$	<b>56.44</b>	33.87	40.83	48.40	<b>82.54</b>	58.66	59.14	64.52
$\theta_1=45^\circ$	<b>40.91</b>	24.68	29.06	39.12	<b>69.89</b>	45.29	56.04	53.68
$\theta_1=60^\circ$	27.20	11.37	19.76	<b>28.84</b>	<b>55.22</b>	23.13	43.90	42.32
V=250 km/h								
	Vertical displacement of the second mid-span of the bridge (mm)				Vertical acceleration of the 1 <sup>st</sup> car-body (cm/s <sup>2</sup> )			
	$\alpha=0$	$\alpha=30^\circ$	$\alpha=60^\circ$	$\alpha=90^\circ$	$\alpha=0$	$\alpha=30^\circ$	$\alpha=60^\circ$	$\alpha=90^\circ$
$\theta_1=30^\circ$	<b>60.24</b>	35.89	45.24	54.18	<b>81.09</b>	55.89	72.51	74.97
$\theta_1=45^\circ$	40.50	23.24	32.00	<b>43.76</b>	<b>74.05</b>	39.42	61.62	63.69
$\theta_1=60^\circ$	27.37	12.60	21.65	<b>32.26</b>	45.78	22.33	42.16	<b>52.89</b>
V=300 km/h								
	Vertical displacement of the second mid-span of the bridge (mm)				Vertical acceleration of the 1 <sup>st</sup> car-body (cm/s <sup>2</sup> )			
	$\alpha=0$	$\alpha=30^\circ$	$\alpha=60^\circ$	$\alpha=90^\circ$	$\alpha=0$	$\alpha=30^\circ$	$\alpha=60^\circ$	$\alpha=90^\circ$
$\theta_1=30^\circ$	<b>63.85</b>	37.88	48.29	58.57	<b>93.54</b>	63.22	58.39	73.55
$\theta_1=45^\circ$	42.88	24.44	33.95	<b>47.34</b>	<b>73.93</b>	61.04	54.73	64.81
$\theta_1=60^\circ$	28.92	13.37	22.88	<b>34.87</b>	49.67	27.57	45.61	<b>51.30</b>
(b) Offload factors and derailment factors								
V=200 km/h								
	Offload factor				Derailment factor			
	$\alpha=0$	$\alpha=30^\circ$	$\alpha=60^\circ$	$\alpha=90^\circ$	$\alpha=0$	$\alpha=30^\circ$	$\alpha=60^\circ$	$\alpha=90^\circ$
$\theta_1=30^\circ$	0.4616	0.3242	0.3764	<b>0.4700</b>	<b>0.3250</b>	0.2743	0.2852	0.3095
$\theta_1=45^\circ$	0.3818	0.2878	0.3182	<b>0.4050</b>	0.2874	0.2643	0.2670	<b>0.3138</b>
$\theta_1=60^\circ$	0.3220	0.2463	0.2735	<b>0.3409</b>	0.2577	0.2611	0.2700	<b>0.3139</b>
V=250 km/h								
	Offload factor				Derailment factor			
	$\alpha=0$	$\alpha=30^\circ$	$\alpha=60^\circ$	$\alpha=90^\circ$	$\alpha=0$	$\alpha=30^\circ$	$\alpha=60^\circ$	$\alpha=90^\circ$
$\theta_1=30^\circ$	<b>0.4729</b>	0.3690	0.4415	0.4300	<b>0.3011</b>	0.2647	0.2753	0.2771
$\theta_1=45^\circ$	0.3682	0.3058	0.3704	<b>0.3743</b>	0.2447	0.2519	<b>0.2972</b>	0.2676
$\theta_1=60^\circ$	<b>0.3111</b>	0.2492	0.2865	0.3052	0.2478	0.2473	<b>0.2988</b>	0.2686
V=300 km/h								
	Offload factor				Derailment factor			
	$\alpha=0$	$\alpha=30^\circ$	$\alpha=60^\circ$	$\alpha=90^\circ$	$\alpha=0$	$\alpha=30^\circ$	$\alpha=60^\circ$	$\alpha=90^\circ$
$\theta_1=30^\circ$	<b>0.4892</b>	0.4149	0.3746	0.4046	0.2789	0.2826	0.2848	<b>0.2883</b>
$\theta_1=45^\circ$	<b>0.4081</b>	0.3327	0.3932	0.3720	0.2898	0.2899	<b>0.3048</b>	0.2978
$\theta_1=60^\circ$	0.3182	0.2879	<b>0.3502</b>	0.3464	0.2677	0.2695	<b>0.3058</b>	0.3044

China Scholarship Council. This study is supported by the National Basic Research Program of China ("973"Project, Grant No. 2013CB036203), the National Natural Science Foundation of China (Grant No. 51508018) and the Fundamental Research Funds for the Central Universities of China (Grant No. 2018JBM037).

## References

- Assimaki, D. and Gazetas, G. (2004), "Soil and topographic amplification on canyon banks and the 1999 Athens earthquake", *J. Earthq. Eng.*, **8**(1), 1-43.
- Assimaki, D. and Jeong, S. (2013), "Ground-motion observations at hotel Montana during the M 7.0 2010 Haiti earthquake:

- Topography or soil amplification?", *B. Seismol. Soc. Am.*, **103**(5), 2577-2590.
- Athanasopoulos, G.A., Pelekis, P.C. and Leonidou, E.A. (1999), "Effects of surface topography on seismic ground response in the Egion (Greece) 15 June 1995 earthquake", *Soil Dyn. Earthq. Eng.*, **18**(2), 135-149.
- Bi, K.M., Hao, H. and Ren, W.X. (2010), "Response of a frame structure on a canyon site to spatially varying ground motions", *Struct. Eng. Mech.*, **36**(1), 111-127.
- Celibi, M. (1987), "Topographical and geological amplifications determined from strong-motion and aftershock records of the 3 March 1985 Chile earthquake", *B. Seismol. Soc. Am.*, **88**(4), 1147-1167.
- Du, X.L. and Zhao, M. (2010), "A local time-domain transmitting boundary for simulating cylindrical elastic wave propagation in infinite media", *Soil Dyn. Earthq. Eng.*, **30**(10), 937-946.
- Du, X.L., Zhao, M. and Wang, J.T. (2006), "A stress artificial boundary in FEA for near-field wave problem", *Chin. J. Theor. Appl. Mech.*, **38**(1), 49-56.
- Du, X.T., Xu, Y.L. and Xia, H. (2012), "Dynamic interaction of bridge-train system under non-uniform seismic ground motion", *Earthq. Eng. Struct. D.*, **41**(1), 139-157.
- Duzgun, O.A. and Budak, A. (2015) "Effects of surface shapes and geotechnical conditions on the ground motion", *KSCE J. Civil Eng.*, **19**(5), 1336-1346.
- Geli, L., Bard, P.Y. and Jullien, B. (1988), "The effect of topography on earthquake ground motion: A review and new results", *B. Seismol. Soc. Am.*, **78**(1), 42-63.
- Jia, H.Y., Zhao, J.G., Li, X., Li, L.P. and Zheng, S.X. (2018), "Probabilistic pounding analysis of high-pier continuous rigid frame bridge with actual site conditions", *Earthq. Struct.*, **15**(2), 193-202.
- Jia, J.F., Song, N.H., Xu, Z.G., He, Z.Z. and Bai, Y.L. (2015), "Structural damage distribution induced by Wenchuan earthquake on 12<sup>th</sup> May, 2008", *Earthq. Struct.*, **9**(1), 93-109.
- Kiureghian, A.D. and Neuenhofer, A. (1992), "Response spectrum method for multi-support seismic excitations", *Earthq. Eng. Struct. D.*, **21**(8), 713-740.
- Liu, J.B., Du, Y.X., Du, X.L., Wang Z.Y. and Wu J. (2006), "3D viscous-spring artificial boundary in time domain", *Earthq. Eng. Eng. Vibr.*, **5**(1), 93-102.
- Lysmer, J. and Kuhlemeyer, R.L. (1969), "Finite dynamic model for infinite media", *J. Eng. Mech.*, **95**(EM4), 759-877.
- Newmark, N.M. (1959), "A method of computation for structural dynamics", *J. Eng. Mech.*, **85**(EM3), 67-94.
- Rassem, M., Ghobarah, A. and Heidebrecht, A.C. (1996), "Site effects on the seismic response of a suspension bridge", *Eng. Struct.*, **18**(5), 363-370.
- Schevenels, M., Francois, S. and Degrande, G. (2009), "EDT: An elastodynamics toolbox for matlab", *Comput. Geosci.*, **35**(8), 1752-1754.
- Smith, W.D. (1975) "The application of finite element analysis to body wave propagation problems", *Geophys. J. Int.*, **42**(2), 747-768.
- Timoshenko, S.P. and Goodier, J.N. (1970), *Theory of Elasticity*, 3rd Edition, McGraw-Hill, New York, U.S.A.
- Tsai, H.C. (1998), "Modal superposition method for dynamic analysis of structures excited by prescribed support displacements", *Comput. Struct.*, **66**(5), 675-683.
- Wang, L., Zhao, C.G. and Qu, T.J. (2008), "Topographic effects on seismic response of long-span rigid-frame bridge under SV seismic wave", *Earthq. Sci.*, **21**(3), 311-318.
- Wang, Z. (2008), "A preliminary report on the great Wenchuan earthquake", *Earthq. Eng. Eng. Vibr.*, **7**(2), 225-234.
- Wilson, E.L. (2002), *Three-Dimensional Static and Dynamic Analysis of Structures: A Physical Approach with Emphasis on Earthquake Engineering*, Computer and Structures Inc., California, U.S.A.
- Xia, H., De Roeck, G. and Goicolea, J.M. (2011), *Bridge Vibration and Controls: New Research*, Nova Science Publishers Inc., New York, U.S.A.
- Xia, H., Han, Y., Zhang, N. and Guo, W.W. (2006), "Dynamic analysis of train-bridge system subjected to non-uniform seismic excitations", *Earthq. Eng. Struct. D.*, **35**(12), 1563-1579.
- Xia, H., Zhang, N. and Gao, R. (2005), "Experimental analysis of railway bridge under high-speed trains", *J. Sound. Vibr.*, **282**(1-2), 517-528.
- Yang, Y.B. and Wu, Y.S. (2002), "Dynamic stability of trains moving over bridges shaken by earthquakes", *J. Sound Vibr.*, **258**(1), 65-94.
- Yau, J.D. and Frýba, L. (2007), "Response of suspended beams due to moving loads and vertical seismic ground excitations", *Eng. Struct.*, **29**(12), 3255-3262.
- Zeng, Q. and Dimitrakopoulos, E.G. (2016), "Seismic response analysis of an interacting curved bridge-train system under frequent earthquakes", *Earthq. Eng. Struct. D.*, **45**(7), 1129-1148.
- Zhang, Z.C., Lin, J.H., Zhang, Y.H., Howson, W.P. and Williams, F.W. (2010a), "Non-stationary random vibration analysis for train-bridge systems subjected to horizontal earthquakes", *Eng. Struct.*, **32**(11), 3571-3582.
- Zhang, N., Xia, H., Guo, W.W. and De Roeck, G. (2010b), "A vehicle-bridge linear interaction model and its validation", *Int. J. Struct. Stab. Dyn.*, **10**(2), 335-361.
- Zhang, C.H., Pan, J.W. and Wang, J.T. (2010c), "Influence of seismic input mechanisms and radiation damping on arch dam response", *Soil Dyn. Earthq. Eng.*, **29**(9), 1282-1293.
- Zhao, J.G., Huang, X.X., Liu, W.F., Zhao W.J., Song, J.Y., Xiong, B. and Wang, S.X. (2017), "2.5-D frequency-domain viscoelastic wave modelling using finite-element method", *Geophys. J. Int.*, **211**(1), 164-187.
- Zhou, C.G. (2009), "Research on the mechanism of seismic wave input about high rockfill dam", M.Sc. Dissertation, Dalian University of Technology, Dalian, China.
- Zhou, G.L., Li, X.J. and Qi, X.J. (2010), "Seismic response analysis of continuous rigid frame bridge considering canyon topography effects under incident SV waves", *Earthq. Sci.*, **23**(1), 53-61.
- Zhu, D.Y., Zhang, Y.H., Kennedy, D. and Williams, F.W. (2014), "Stochastic vibration of the vehicle-bridge system subjected to non-uniform ground motions", *Vehic. Syst. Dyn.*, **52**(3), 410-428.

CC